Influence of electronic exchange on single and multiple processes in collisions between bare ions and noble-gas atoms

T. Kirchner,[1] L. Gulyás,[2] H. J. Lüdde,[1] E. Engel,[1] and R. M. Dreizler[1]

[1]*Institut für theoretische Physik, Universität Frankfurt, Robert-Mayer-Straße 8, D-60054 Frankfurt/Main, Germany*
[2]*Institute of Nuclear Research of the Hungarian Academy of Sciences (ATOMKI), P.O. Box 51, H-4001 Debrecen, Hungary*

The time-dependent many-electron problem encountered in the theory of energetic ion-atom collisions can be approached systematically within an effective single-particle picture, based, e.g., on the time-dependent density functional theory. In the present contribution we investigate ionization and electron loss from the target for the collision systems p, $\bar{p}$, $He^{2+} + Ne$, and $p + Ar$ in the energy range 10 keV/amu–1 MeV/amu. The results presented are based on a static approximation to the exchange-correlation contribution of the effective potential. The corresponding time-dependent single-particle equations are solved with the *continuum distorted-wave with eikonal initial-state* approximation and the *basis generator method*, a coupled-channel approach in terms of structurally adapted basis functions. We demonstrate that in either case the results depend strongly on the explicit form of the local static exchange potential. An orbital-dependent analysis of electron removal in $He^{2+} + Ne$ collisions shows that the quality of the exchange potential is decisive for the suppression of artificial reaction channels. [S1050-2947(98)05309-8]

PACS number(s): 34.50.Fa, 34.70.+e

I. INTRODUCTION

Various features of collisions between bare ions and noble-gas atoms have been the subject of experimental studies, with the aim to provide a quantitative understanding of many-electron dynamics. The data available at present contain information on differential and total ionization yields [1–3] and multiple ionization and charge-transfer processes, as well as details of the momentum distributions of the participating particles [4,5].

In the case of helium targets many of the experimental results have been analyzed with the aid of both classical and quantum mechanical calculations. In particular, the role of the electron-electron interaction in multiple transition processes like double ionization has been investigated in some detail [6,7].

By contrast, the current understanding of experimental data for targets involving more than two active electrons is mainly guided by (quasi)classical descriptions of the electronic motion in phase space [8] and statistical treatments based on the energy deposition model [9]. Notwithstanding the partial success of these approximations (see, e.g., Ref. [4]) theoretical methods based on quantum mechanics are desirable not only as a matter of principle but also for the practical purpose of a quantitative understanding of the experimental results. For example, it has recently been shown that multiple-capture cross sections in fast $Ar^{q+} + Ar$ collisions obtained with a variant of the Vlasov ($\hbar = 0$) model are in marked disagreement with experimental data [10]. One may suppose that the quantum character of the many-electron system is decisive for multiple-capture processes, since the Pauli exclusion principle has to be considered. Moreover, we have recently shown [11] that even global ionization cross sections at high impact energies are influenced by electronic exchange effects, which cannot be taken into account in a consistent way in classical methods.

The few quantum-mechanical approaches, beyond the first Born approximation, for many-electron scattering systems have been restricted to distorted-wave theories for one-electron ionization [12–14] and to an application of the time-dependent Feshbach formalism [15]. They rely on an effective single-particle picture. This picture can be justified by time-dependent density-functional theory (TDDFT), which ensures the existence of an exact mapping of the true many-body problem to an effective single-particle description, in which a multiplicative single-particle potential accounts for all electron-electron interaction effects [16,17]. Therefore, the correlated time-dependent many-electron problem can be approached systematically by appropriate approximations of this effective potential.

In this paper, we compare the influence of static exchange effects obtained with different potentials on inelastic collision processes. The time dependence of these potentials, due to the response of the density in the presence of the projectile, is neglected. We utilize two different methods for the solution of the single-particle equations, both of which have demonstrated their reliability in pure one-electron scattering problems. The *continuum distorted-wave with eikonal initial-state* (CDW-EIS) approximation introduced by Crothers and McCann [18] is well suited for a description of ionization cross sections, differential in emission energy and angle at intermediate and high impact energies [19], while the *basis generator method* (BGM), a coupled-channel approach introduced recently [20,21], has been shown to be competitive with large-scale calculations in describing excitation, ionization, and capture over a wide range of energies [22]. Taking advantage of the capabilities of both methods, we investigate electron-electron interaction effects from different viewpoints and for different scattering situations.

The paper is organized as follows. After a brief outline of the general theory, in Sec. II A we discuss the properties of the single-particle potentials used. In Sec. II B, we address

the question of how to extract many-electron observables from the solutions of the single-particle equations. The CDW-EIS and BGM methods are briefly reviewed in Sec. II C. Results are presented in Sec. III. We discuss static potential effects on energy and angular distributions of continuum electrons in $p+$Ne and $p+$Ar collisions (Sec. III A), and on capture processes in He$^{2+}+$Ne collisions (Sec. III B). In addition, results for ionization of Ne by antiprotons are presented in Sec. III C. We conclude with a summarizing discussion in Sec. IV. Atomic units are used throughout.

II. THEORY

Within the semiclassical approximation the discussion of ion-atom scattering processes starts from the many-electron Hamiltonian

$$\hat{H}(t) = \sum_{i=1}^{N} \left(-\frac{1}{2}\Delta_i - \frac{Q_T}{r_i} - \frac{Q_P}{|\boldsymbol{r}_i - \boldsymbol{R}(t)|} \right) + \sum_{i<j}^{N} \frac{1}{|\boldsymbol{r}_i - \boldsymbol{r}_j|}. \tag{1}$$

Q_T and Q_P denote the charges of target and projectile nuclei, respectively, $\boldsymbol{r}_i$ is the position vectors of the electrons with respect to the target center, and $\boldsymbol{R}(t)$ is the classical nuclear trajectory, which carries explicit time dependence into the problem. Here we assume a straight line $\boldsymbol{R}(t)=(b,0,vt)$ with constant velocity v and impact parameter b. In order to cope with collision systems involving more than two active electrons, we rely on an effective single-particle picture, which can be rigorously based on TDDFT. This formalism (with suitable representability conditions) ensures the existence of a local (multiplicative) single-particle potential v_{ee} which, provided that the system is in its ground state at the beginning, is a functional of the exact one-particle density

$$n(\boldsymbol{r},t) = \sum_{i=1}^{N} |\psi_i(\boldsymbol{r},t)|^2. \tag{2}$$

The orbitals $\{\psi_i\}$ are solutions of the time-dependent Kohn-Sham (TDKS) equations

$$i\partial_t \psi_i(\boldsymbol{r},t) = \hat{h}(t)\psi_i(\boldsymbol{r},t), \quad i=1,\ldots,N \tag{3}$$

with the single-particle Hamiltonian

$$\hat{h}(t) = -\frac{1}{2}\Delta - \frac{Q_T}{r} - \frac{Q_P}{|\boldsymbol{r}-\boldsymbol{R}(t)|} + v_{ee}([n(t)];\boldsymbol{r},t). \tag{4}$$

Since, in principle, the time-dependent quantum-mechanical state is uniquely determined by $n(\boldsymbol{r},t)$ [16,17], i.e., can be expressed as a functional of density (2), the scheme indicated is formally equivalent to solving the full many-body problem governed by the Hamiltonian (1).

Usually, v_{ee} is decomposed into time-dependent Hartree and time-dependent exchange-correlation parts. Although the latter can be expressed exactly in terms of a perturbation series [23], approximations have to be introduced for practical applications [17,24].

Here we do not attempt to tackle this demanding problem. Since we consider *energetic* collisions with bare projectiles, a simpler approximation should be justified: We decompose v_{ee} according to

$$v_{ee}([n(t)];\boldsymbol{r},t) = v_{ee}([n];\boldsymbol{r}) + \delta v_{ee}([n(t)];\boldsymbol{r},t), \tag{5}$$

where $n(\boldsymbol{r})=n(\boldsymbol{r},t_0)$ is the ground-state density of the unperturbed atomic target, and δv_{ee} the variation of v_{ee} due to the response of the density in the presence of the projectile. For fast collisions the response part may be neglected, since the spatial electronic distribution does not change considerably during the interaction time,

$$\delta v_{ee}([n(t)];\boldsymbol{r},t) \approx 0. \tag{6}$$

In a recent publication [11], we showed that this approximation allows a precise calculation of total cross sections for net electron loss and ionization if the frozen atomic potential $v_{ee}([n];\boldsymbol{r})$ accounts accurately for electronic exchange effects.

A. Atomic potentials

For the effective Kohn-Sham (KS) potential v_{KS} of stationary systems,

$$v_{KS}([n];\boldsymbol{r}) = v_{ext}(\boldsymbol{r}) + v_{ee}([n];\boldsymbol{r}), \tag{7}$$

where the external potential v_{ext} is the Coulomb potential of the target nucleus in our particular case, a variety of approximations has been introduced. Extracting its exchange-correlation (xc) component by subtraction of the Hartree potential,

$$v_{xc}([n];\boldsymbol{r}) = v_{ee}([n];\boldsymbol{r}) - v_H([n];\boldsymbol{r}), \tag{8}$$

$$v_H([n];\boldsymbol{r}) = \int d^3r' \frac{n(\boldsymbol{r}')}{|\boldsymbol{r}-\boldsymbol{r}'|}, \tag{9}$$

two basic DFT concepts for the treatment of v_{xc} can be distinguished.

In the traditional scheme v_{xc} is approximated as an explicit functional of the density. The two best-known xc potentials of this type are the local-density approximation (LDA) [25] and the Hartree-Fock-Slater (HFS) [26] potentials. In the former the density dependence of the xc potential of the homogeneous electron gas (HEG) is used for the actual local density of the inhomogeneous system of interest,

$$v_{xc}^{LDA}([n];\boldsymbol{r}) = v_{xc}^{HEG}(n(\boldsymbol{r})) = \frac{de_{xc}^{HEG}(n_0)}{dn_0}\bigg|_{n_0=n(\mathbf{r})}, \tag{10}$$

where $e_{xc}^{HEG}(n_0)$ is the xc energy density of a HEG with density n_0. Separating the exchange (x) from the correlation (c) part, the former is given by

$$v_x^{LDA}(n) = -\frac{(3\pi^2 n)^{1/3}}{\pi}, \tag{11}$$

while for the latter only accurate analytic interpolation formulas for the numerically evaluated $v_c(n_0)$ are available

(e.g., Ref. [27]). The HFS potential, on the other hand, is given by the average exchange interaction energy of a single electron in the HEG with all others,

$$v_{xc}^{HFS}(n) = \tfrac{3}{2}\, v_x^{LDA}(n).\qquad(12)$$

2It should be emphasized that from a DFT point of view the LDA is a consistent *first principles* approximation, as it is derived from the xc energy functional $E_{xc}[n]$ of the HEG via $\delta E_{xc}[n]/\delta n(r)$, in contrast to the HFS potential. In addition, the LDA proved to be superior to the HFS approximation for a large variety of systems [28], so that in the context of DFT the HFS potential (12) is only used in the framework of the $X\alpha$ approximation, i.e., with a prefactor α close to $\tfrac{2}{3}$.

The LDA and, in particular, the HFS scheme are often modified *a posteriori* in order to account for the fact that the exact atomic v_x exhibits a $-1/r$ tail in the asymptotic regime [29], rather than the exponential decay observed for v_x^{LDA},

$$v_{xc}^{LDA/L}(n) = \begin{cases} v_{xc}^{LDA}(n) & \text{for } v_{xc}^{LDA}(n) < -1/r \\ -1/r & \text{elsewhere.} \end{cases}\qquad(13)$$

This ''latter correction'' is used throughout the present work, i.e., we will identify the LDA/L with the LDA in the following (analogously for the HFS approximation).

As a refined form of explicit density functionals generalized gradient approximations (GGA's) [30], in which in addition to n ∇n is also used to represent the exchange-correlation energy, have been extensively used during the last years. However, while GGA's were shown to improve the global description of atomic, molecular, and condensed-matter systems (see, e.g., Ref. [31]), these semilocal functionals do not resolve some fundamental deficiencies of the LDA, most notably its incomplete cancellation of the self-interaction contained in the Hartree energy and the associated incorrect asymptotic behavior of v_x. As the latter property is of particular importance for the discussion of scattering problems, GGA's cannot be considered a real alternative in the present context.

A *first-principles* DFT scheme, in which the self-interaction energy can be treated exactly, is provided by the optimized potential method (OPM). In this case the xc energy is represented in terms of the KS orbitals φ_i, which themselves are unique functionals of n [32]. In the case of the exchange one usually applies the standard Fock expression,

$$E_x = -\frac{1}{2}\int d^3r \int d^3r' \sum_{\epsilon_k,\epsilon_l \le \epsilon_F} \frac{\varphi_k^*(r)\varphi_l(r)\varphi_l^*(r')\varphi_k(r')}{|r-r'|},\qquad(14)$$

where ϵ_k are the KS eigenvalues (the KS single-particle levels are occupied up to the Fermi level ϵ_F). This E_x exactly cancels the self-interaction of the individual orbitals in the Hartree contribution, and thus ensures the correct asymptotic behavior of v_x.

For the correlation energy, on the other hand, systematically derived functionals have only recently been suggested [33]. The only functional available in practice is the empirical form of Colle and Salvetti [34], which we have also used throughout the present work.

As a consequence of the implicit density dependence of the xc energy, the corresponding xc potential

$$v_{xc}(r) = \frac{\delta E_{xc}[\varphi_i]}{\delta n(r)} = \int d^3r' \, \frac{\delta v_{KS}(r')}{\delta n(r)}$$

$$\times \int d^3r'' \sum_k \frac{\delta \varphi_k^*(r'')}{\delta v_{KS}(r')} \frac{\delta E_{xc}[\varphi_i]}{\delta \varphi_k^*(r'')} + \text{c.c.}$$

has to be evaluated indirectly via the OPM integral equation [35,36]

$$\int d^3r' \frac{\delta n(r)}{\delta v_{KS}(r')} v_{xc}(r')$$

$$= \sum_{k,l\ne k} \int d^3r' \varphi_k^*(r) \frac{\varphi_l(r)\varphi_l^*(r')}{\epsilon_k - \epsilon_l} \frac{\delta E_{xc}}{\delta \varphi_k^*(r')} + \text{c.c.}$$

$$(15)$$

Although the numerical solution of Eq. (15) is rather involved, the OPM has attracted considerable interest during the last years [37], as applications to atoms [36,38] have demonstrated that this approach is superior to the conventional LDA or GGA and yields in its exchange-only version nearly equal results as full Hartree-Fock calculations.

The total LDA, HFS, and OPM KS potentials for neutral Ar are shown in Fig. 1. Also indicated are the orbital binding energies ϵ_i of the $3s$ and $3p$ wave functions. It is obvious that the three potentials differ considerably: In the valence regime around $r=1$ a.u., the differences between the LDA and HFS potential are of the order of 100 mhartree, the differences between the HFS and OPM potentials become as large as 200 mhartree. Correspondingly one finds $3p$ eigenvalues of -429 mhartree for the LDA, -533 mhartree for the HFS approximation, and -620 mhartree in the case of the OPM. One also observes explicitly the sudden switching of the LDA and HFS potentials to the $-1/r$ behavior. The OPM potential, on the other hand, approaches this limit much more smoothly.

Note that the experimental ionization potential of Ar is -579 mhartree, while the corresponding x-only eigenvalue is -591 mhartree [36]. Thus for Ar the exact v_c is repulsive in the valence region, indicating that the Colle-Salvetti cor-
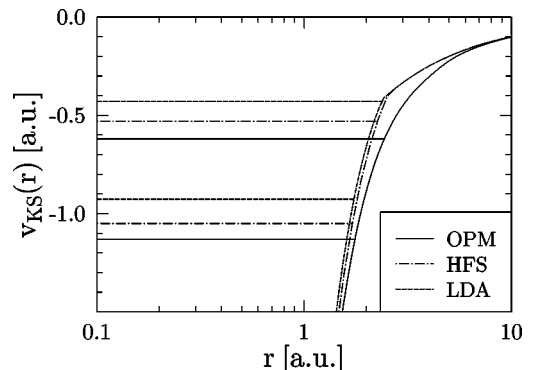

FIG. 1. Kohn-Sham (KS) potentials for neutral Ar. The horizontal lines indicate the orbital binding energies of the $3s$ and $3p$ wave functions.

relation potential has an incorrect sign in this regime. The same is true in the case of the LDA, for which, however, this problem is masked by the much less attractive v_x (see also Ref. [39]). As presently no correlation functional which gives repulsive v_c's for the noble gases is available, the error introduced by this part of v_{xc} is unavoidable, as long as one does not want to neglect v_c completely.

B. Extraction of many-particle probabilities

Within the framework of TDDFT the basic quantity is the one-particle density [Eq. (2)]. Thus, it is desirable to relate the specific many-particle observables of interest directly to it. This is straightforward for net electron loss (Sec. II B 1), but in general the functional dependence of many-particle probabilities on $n(\mathbf{r},t)$ is not known. However, the solution of the TDKS equations (3) provides a set of quantities which are unique functionals of $n(\mathbf{r},t)$, i.e., the KS orbitals ψ_i. While the explicit functional dependence of the ψ_i on n is not available, any quantity which can be expressed in terms of the ψ_i can thus also be understood as a functional of n. In addition, as we do not take into account time-dependent correlation effects [Eq. (6)], and the correlation contribution in $v_{ee}([n];\mathbf{r})$ is of minor importance for the collision problems considered, it is well justified to attribute direct physical significance to the Kohn-Sham orbitals and approximate the N-electron wave function by a *single* Slater determinant constructed from them. Multiple-electron transitions (Sec. II B 2) can then be calculated without further simplifications on the basis of inclusive probability theory [40–42]. In order to be consistent with assumption (6), we analyze the N-electron wave function with respect to asymptotic single-particle states determined by the Hamiltonian of the undisturbed atomic system. Although this procedure is well defined it is not unique, and may be questionable in particular if transition probabilities to many-electron states corresponding to high degrees of ionization are calculated. This ambiguity is related to the well-known difficulties of time-dependent Hartree Fock theory, which would become apparent in our description, if we would include a time-dependent response potential.

1. Net electron loss and ionization

We define net electron loss P_{net} as the average number of electrons ejected from the target atom in the course of the scattering process. After the collision $(t\rightarrow\infty)$ the part of the electronic density that has been removed from the target is well separated in space from the remainder. One can find a surface $S(T)$ of zero density flux,[1] that encloses the target T, and obtains P_{net} by integrating the density over the outer region of space I:

$$P_{net}=\int_I n(\mathbf{r},t\rightarrow\infty)d^3r=N-\int_T n(\mathbf{r},t\rightarrow\infty)d^3r. \quad (16)$$

---

[1]The zero flux surface can be defined in terms of the density as $\mathbf{e}\cdot\nabla n(\mathbf{r},t\rightarrow\infty)=0$ for all points on S where $\mathbf{e}$ is a vector of unit length perpendicular to S.

Instead of performing the integration in space, one can switch to a channel representation of I in terms of one-particle orbitals $\{|f\rangle\}$ that vanish in T. One then finds

$$P_{net}=\sum_f \sum_i^N |c_f^i|^2, \quad (17)$$

$$c_f^i=\langle f|\psi_i(t\rightarrow\infty)\rangle. \quad (18)$$

As the net electron loss is a measure of the total production of positive charge in the target atom, it includes all electron transfer and ionization channels. However, at high impact energies and for low projectile charges the contribution of capture processes is negligible, and P_{net} corresponds to the average number of electrons promoted to the continuum (net ionization).

2. Multiple-electron loss and ionization

The starting point for the calculation of quantities that refer to the observation of only q particles of the N-particle system is the concept of reduced density matrix. The probability of finding q electrons at specific positions with defined spin, while nothing is known about the remaining $N-q$ electrons, is determined by the diagonal elements

$$\gamma^q(x_1\cdots x_q)=\binom{N}{q}\int d^4x_{q+1}\cdots d^4x_N|\Psi(x_1\cdots x_N)|^2 \quad (19)$$

of the q-particle density matrix, weighted with the corresponding one-particle volumes d^4x_j (x_j denotes space and spin coordinates of the jth electron). As soon as the N-electron wave function Ψ is approximated by a single Slater determinant constructed from the solutions of Eqs. (3), one finds

$$\gamma^q(x_1\cdots x_q)=\frac{1}{q!}\begin{vmatrix} \gamma^1(x_1,x_1) & \cdots & \gamma^1(x_1,x_q) \\ \vdots & \ddots & \vdots \\ \gamma^1(x_q,x_1) & \cdots & \gamma^1(x_q,x_q) \end{vmatrix}, \quad (20)$$

$$\gamma^1(x_1,x_2)=\sum_{i=1}^N \phi_i(x_1)\phi_i^*(x_2), \quad (21)$$

with the spin orbitals

$$\phi_i(x)=\psi_i(\mathbf{r})\chi_{\sigma_i}(s) \quad (22)$$

and the standard spin functions

$$\chi_{1/2}(s)=\begin{pmatrix}1\\0\end{pmatrix}, \quad \chi_{-1/2}(s)=\begin{pmatrix}0\\1\end{pmatrix}. \quad (23)$$

The density of any order q is thus determined by the KS orbitals and thus by the density. The fact that one has to calculate a determinant reflects the effect of the Pauli principle.

Accordingly, if one switches to a final channel representation of the one-particle density matrix in terms of spin orbitals $\{|\tilde{f}\rangle\}$, the inclusive probability of finding q electrons in the subconfiguration $|\tilde{f}_1\cdots\tilde{f}_q\rangle$ (represented by a Slater

determinant), while the remaining $N-q$ electrons occupy arbitrary other one particle states, is given as the $q \times q$ determinant [40]

$$P_{\tilde{f}_1 \cdots \tilde{f}_{q\,\Sigma}} = \det(\langle \tilde{f}_i | \hat{\gamma}^1(t \to \infty) | \tilde{f}_j \rangle). \qquad (24)$$

The probability P_q of finding exactly q electrons in any of the states that correspond to electron loss, while $N-q$ electrons remain bound to the target, can be expressed in terms of the simple inclusive probabilities (24)

$$P_q = \sum_{k=0}^{N-q} (-1)^k \binom{q+k}{k} \sum_{\tilde{f}_1 < \cdots < \tilde{f}_{q+k}} P_{\tilde{f}_1 \cdots \tilde{f}_{q+k}\Sigma}, \quad (25)$$

where the ordered sum has to be taken over all electron loss states.

The evaluation of q-fold loss is considerably simplified if one neglects the Pauli principle and follows the statistical approach [43]. Starting from single-electron-loss probabilities p_i, defined as

$$p_i = \sum_f |c_f^i|^2, \qquad (26)$$

P_q is obtained according to

$$P_q = \sum_{q_1, \cdots, q_m = 0, \Sigma_{i=1}^m q_i = q}^{N_1, \cdots, N_m} \prod_{i=1}^m \binom{N_i}{q_i} p_i^{q_i} (1-p_i)^{N_i - q_i}. \qquad (27)$$

Here, m is the number of electron shells, and N_i the number of electrons in each shell. If one furthermore introduces the average single-electron-loss probability

$$p = \frac{1}{N} \sum_{i=1}^N p_i, \qquad (28)$$

one arrives at the simple binomial formula

$$P_q = \binom{N}{q} p^q (1-p)^{N-q}, \qquad (29)$$

which has been widely used for the calculation and analysis of multiple-ionization processes [44,45]. Although the q-fold loss probabilities P_q calculated from Eqs. (25), (27), and (29) in general differ due to the effects of the Pauli principle and the electronic shell structure, one can show that their average values equal the net electron loss P_{net} (17),

$$P_{\text{net}} = \sum_{q=1}^N q P_q. \qquad (30)$$

C. Solution of the single-particle equations

With approximation (6), the single-particle Hamiltonian (4) can be split into stationary and time-dependent parts

$$\hat{h}(t) = \hat{h}_0 + \hat{v}(t), \qquad (31)$$

$$\hat{h}_0 = -\frac{1}{2}\Delta - \frac{Q_T}{r} + v_{\text{ee}}([n];r), \qquad (32)$$

$$\hat{v}(t) = \frac{-Q_P}{|r - R(t)|}. \qquad (33)$$

In order to solve the time-dependent equations (3) for Hamiltonian (31) for each initially occupied orbital, we apply the CDW-EIS approximation and the BGM.

1. CDW-EIS

Distorted-wave theories are introduced to represent some physical features of the collision in the channel wave functions. The essence of the continuum distorted-wave (CDW) model is to treat some parts of the kinetic energy as perturbation, and to allow for the effects of the potential in the channel wave functions. The distorted-channel wave functions are expressed as products of unperturbed atomic orbitals and a Coulomb distortion factor including the effect of the interaction potential. However, application of the first-order term in the perturbative series (called also CDW) to describe the ionization of hydrogen by proton impact showed that the theory overestimates the experiment at intermediate impact energies [46]. This failure was attributed to the incorrect normalization of the initial distorted-wave function and was corrected by Crothers and McCann [18] by using the eikonal approximation to the Coulomb distorted wave in the initial channel, the CDW-EIS model. In this first-order model the initial, eikonal, distorted-wave function is

$$\chi_i^+ = \alpha_i^+(s) \varphi_i(r) e^{-i\epsilon_i t},$$

$$\varphi_i(r) = \frac{u_{n_i l_i}(r)}{r} Y_{l_i}^{m_i}(\hat{r}), \qquad (34)$$

$$\alpha_i^+(s) = \exp[-i\nu \ln(q_v)],$$

where $\nu = Q_P/v$, $q_v = vs + v \cdot s$ and $s = r - R$ denotes the position vector of the electron with respect to the projectile. The final, Coulomb distorted wave function is

$$\chi_f^- = \alpha_f^-(s) \varphi_\epsilon^-(r) e^{-i\epsilon t},$$

$$\alpha_f^-(s) = N^*(\zeta) {}_1F_1(-i\zeta; 1; -iq_p), \qquad (35)$$

where $N(\zeta) = \exp(\pi\zeta/2)\Gamma(1+i\zeta)$, $\zeta = Q_P/p$, $q_p = ps + p \cdot s$, $p = k - v$, and k (p) is the ejected electron momentum in the target (projectile) frame. The functions φ_i and φ_ϵ^- are the bound and continuum eigenstates of the target Hamiltonian with energy ϵ_i and $\epsilon = k^2/2$, respectively. The continuum eigenstate can be given in the partial wave expansion

$$\varphi_\epsilon^-(r) = \frac{1}{r\sqrt{k}} \sum_{lm} i^l e^{-i\delta_l} u_{\text{el}}(r) [Y_l^m(\hat{r})]^* Y_l^m(\hat{k}), \quad (36)$$

normalized on the energy scale through the condition

$$u_{\epsilon l}(r) \xrightarrow{r \to \infty} \sqrt{\frac{2}{\pi k}} \sin\left(kr + \frac{1}{k}\ln(2kr) - \frac{l\pi}{2} + \delta_l\right), \qquad (37)$$

where δ_l denotes the phase shift. The states χ_i^+ and χ_f^- satisfy the correct Coulomb boundary conditions and describe the ejected electron as moving in the combined Cou-

lomb field of the target and projectile nuclei. The latter is important in order to account for two-center effects (TCE's) [47]. The model was extended to multielectronic targets in Ref. [48]. In an effective single-particle picture, Roothan-Hartree-Fock [49] and screened H-like orbitals were used for the initial and final channels, respectively. Recently the model of Ref. [48] was generalized in Ref. [14]: the bound and continuum states of the target were obtained by solving numerically the time-independent Schrödinger equation with the Hamiltonian (32) for a given single-particle potential. In this way the initial and final orbitals of the target are, by definition, orthogonal, which was not the case in the previous version. The nonorthogonality of the orbitals leads to an underestimation of the electron emission in the backward direction, as discussed in Ref. [50] in the framework of the first Born model.

The transition amplitude as a function of impact parameter $\boldsymbol{b}$ can be expressed as

$$a_{if}(\boldsymbol{b}) = -i \int_{-\infty}^{+\infty} dt \langle \chi_f^- | (\hat{h} - i\partial_t) | \chi_i^+ \rangle$$

$$= \frac{1}{2\pi} \int d\boldsymbol{\eta} e^{-i\boldsymbol{\eta}\cdot\boldsymbol{b}} R_{if}(\boldsymbol{\eta}), \qquad (38)$$

where $\boldsymbol{\eta}$ denotes the transverse momentum transfer. The advantage of the CDW methods is the fact that R_{if} (transition amplitude as a function of $\boldsymbol{\eta}$) can be given in analytic form, which was used previously in calculating the cross sections [14]. Recently the authors of Ref. [51] evaluated the two-dimensional Fourier transform in Eq. (38) numerically in order to calculate single-ionization probabilities. The probability of finding an electron in the continuum with energy ϵ and in the direction Ω_ϵ is expressed as

$$\frac{dp_i(b)}{d\epsilon\, d\Omega_\epsilon} = \frac{1}{2\pi} \int_0^{2\pi} d\varphi_b |a_{if}(\boldsymbol{b})|^2 = \sum_{mm'} \sum_{\mu=-\infty}^{+\infty} \sum_{\mu'=-\infty}^{+\infty} S_{m,\mu}(b)$$

$$\times S_{m',\mu'}^*(b)\delta_{m+\mu,m'+\mu'}, \qquad (39)$$

where φ_b is the azimuthal angle of $\boldsymbol{b}$. For details on $S_{m,\mu}$ and on the transition amplitudes, the reader is referred to Refs. [14,51]. The terms with $\mu \neq 0$ are related to the distortion effects of the projectile on the electronic structure. The first Born approximation ($B1$) can be obtained by neglecting the distortions in the channel wave functions [$Q_P = 0$ in Eqs. (34) and (35)], consequently only the term $\mu = 0$ survives in Eq. (39). The single-particle probability p_i for ionization of an electron from a given initial state can be obtained by integrating Eq. (39) over the coordinates of the ejected electrons.

2. Basis generator method (BGM)

Coupled-channel methods rely on a representation of the solution of time-dependent quantum problems within a *finite model space*. We start by selecting a set of bound eigenstates $\{|\varphi_s^0\rangle, s=1,\dots,L\}$ of the undisturbed atomic Hamiltonian $\hat{h}_0$ [Eq. (32)], which includes the initially occupied orbitals.

A hierarchy of finite subspaces is then generated by repeated application of the Schrödinger operator $\hat{h}(t) - i\partial_t$ on these functions:

$$|\varphi_s^\mu\rangle = (\hat{h}(t) - i\partial_t)|\varphi_s^{\mu-1}\rangle = (\hat{h}(t) - i\partial_t)^\mu |\varphi_s^0\rangle,$$

$$s = 1,\dots,L, \quad \mu = 1,\dots,M. \qquad (40)$$

In Ref. [20], we showed that only states of the highest order $\mu = M$ couple to the part of the Hilbert space that is not included in the basis. If these states are not accessed during the collision, the representation of the solution of Eq. (3) in terms of the hierarchy is exact.

It is a formidable task to construct the states $|\varphi_s^\mu\rangle$ explicitly, as the repeated application of the Laplacian in Eq. (31) leads to complicated gradient terms with increasing order μ. Therefore, we establish a different strategy in Ref. [21]: the *basis generator method* (BGM). The gist of the BGM is the construction of a finite model space from different states $|\chi_s^\mu\rangle$, whose generation is less involved, in order to represent each state $|\varphi_s^\mu\rangle$ as a linear combination of the former. Thus, the hierarchy $\{|\varphi_s^\mu\rangle, s=1,\dots,L, \mu=0,\dots,M\}$ is embedded in the new model space generated by the set $\{|\chi_s^\mu\rangle, s=1,\dots,L', \mu=0,\dots,M'\}$, and the advantageous properties of the basis are maintained.

For the two-center Coulomb problem with the Hamiltonian

$$\hat{h}(t) = -\frac{1}{2}\Delta - \frac{Q_T}{r} - \frac{Q_P}{|\boldsymbol{r}-\boldsymbol{R}(t)|}, \qquad (41)$$

a basis $\{|\chi_s^\mu\rangle\}$ with the required properties can be found if one relies on a particular regularization of the Coulomb potential. Regularization procedures are necessary in order to avoid divergent matrix elements, and have been discussed in a previous publication [52]. Using the ansatz

$$\hat{v}(t) = \frac{-Q_P}{|\boldsymbol{r}-\boldsymbol{R}(t)|} = -Q_P \lim_{\varepsilon\to 0} W_P(\varepsilon),$$

$$W_P(\varepsilon) = [(x-X)^2 + y^2 + (z-Z)^2 + \varepsilon^2]^{-1/2},$$

$$\hat{v}_0 = -\frac{Q_T}{r} = -Q_T \lim_{\varepsilon_0\to 0} W_0(\varepsilon_0), \qquad (42)$$

$$W_0(\varepsilon_0) = [r^2 + \varepsilon_0^2]^{-1/2} \equiv \frac{1}{r_{\varepsilon_0}},$$

the BGM basis functions can be expressed as

$$\chi_{nlm}^\mu(\boldsymbol{r}; \xi, \varepsilon_0, \varepsilon) = [W_P(\varepsilon)]^\mu \chi_{nlm}^0(\boldsymbol{r}; \xi, \varepsilon_0),$$

$$\chi_{nlm}^0(\boldsymbol{r}; \xi, \varepsilon_0) = r_{\varepsilon_0}^{n-1} e^{-\xi r_{\varepsilon_0}} \left(\frac{r}{r_{\varepsilon_0}}\right)^l Y_l^m(\theta, \varphi), \quad n \in \mathcal{Z}.$$

$$(43)$$

If the states $\{\chi_{nlm}^0(\xi, \varepsilon_0)\}$ are replaced by the eigenfunctions $\{\phi_{nlm}^0\}$ of the Hamiltonian $\hat{h}_0$ [Eq. (32)], one arrives at the approximate construction scheme

$$\chi^{\mu}_{nlm}(\mathbf{r};\varepsilon) = [W_P(\varepsilon)]^{\mu} \varphi^0_{nlm}(\mathbf{r}), \qquad (44)$$

that has been discussed and applied in previous publications in a different context [20,22]. For practical applications it is more convenient to use BGM states that are orthogonal to the set of eigenstates $|\varphi^0_s\rangle$. This can be achieved with the polynomial ansatz [20]

$$|\chi^{\mu}_s\rangle = \sum_{\lambda=0}^{\mu} [W_P]^{\lambda} \sum_{s'=1}^{L} a^{\mu,\lambda}_{s,s'} |\varphi^0_{s'}\rangle. \qquad (45)$$

Equations (3) are solved by expansion in terms of these basis functions

$$|\psi_i(t)\rangle = \sum_{\mu=0}^{M} \sum_{s=1}^{L} c^i_{\mu,s}(t) |\chi^{\mu}_s(t)\rangle. \qquad (46)$$

If the set of eigenstates $\{|\varphi^0_s\rangle\}$ includes the important elastic and target excitation channels the BGM states represent electron loss. Thus information about many-particle loss can be obtained from their occupation for $t \to \infty$, as described in Sec. II B.

III. RESULTS AND DISCUSSION

In a recent publication [11], we showed that both methods, CDW-EIS and BGM, reveal a strong dependence of total cross sections (TCS's) for net electron loss on the explicit form of the atomic exchange potential inserted in Eq. (32). At high impact energies both methods give comparable results if the same potential is used. Here we extend the investigation of static potential effects in order to provide additional information concerning their role in inelastic collision processes.

The energy and angular distribution of electrons ejected from the target can be studied with the CDW-EIS method at sufficiently high impact velocities. Corresponding results for $p + \text{Ne}$ and $p + \text{Ar}$ collisions are presented in Sec. III A. The BGM also permits a calculation of cross sections at lower impact energies where capture processes contribute significantly to electron loss, if bound projectile states exist. We analyze the influence of exchange effects on these processes for $\text{He}^{2+} + \text{He}$ collisions in Sec. III B. Finally, we apply both methods to the scattering system $\bar{p} + \text{Ne}$, for which ionization TCS's have been measured very recently [53].

A. Energy and angular distribution of ionized electrons

The study of differential electron ejection is expected to provide more sensitive tests of the adequacy of the different single-particle potentials than the TCS's. In this section we present results for single differential cross sections (SDCS's) and for angular asymmetry parameters. These quantities are calculated for 300-keV $\text{H}^+ + \text{Ne}$, Ar collisions in the CDW-EIS approximation, applying different single-particle potentials (OPM, LDA, and HFS). At this collision energy the ionization yields are dominated by the ejection of electrons from the outer shells: the $n = 2$ and 3 levels of Ne and Ar atoms, respectively. These outer orbitals evaluated with the
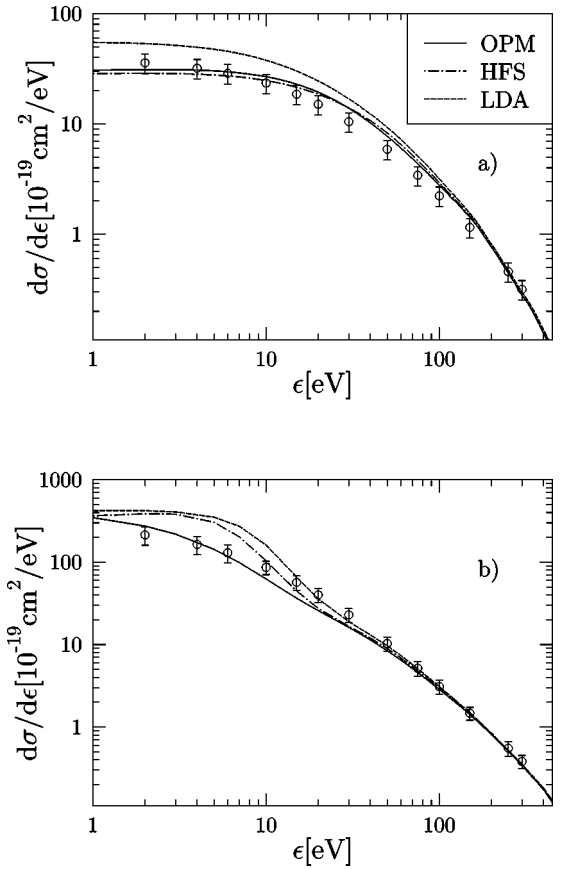

FIG. 2. Single-differential cross section (SDCS) as a function of electron energy for 300-keV H^+ impact on (a) Ne and (b) Ar. Lines: CDW-EIS calculation with different atomic potentials; ($\bigcirc$) experimental data taken from Ref. [2].

different potentials exhibit different binding energies that deviate by about 20–40 % (cf. Fig. 1) and slightly varying shapes.

Different regions of the differential electron distribution can be attributed to different collision mechanisms [1]. The two fundamental ones, giving the most important contribution to the total electron yields, are soft and hard collision processes. Soft collisions are characterized by small momentum and energy transfer in contrast to hard or binary collisions which are dominated by large momentum transfer, and result in high-energy electron emission. Accordingly, soft collisions take place at large impact parameters and transfer of unit angular momentum is the most probable $[|l,l'-l_i|=1$; see Eq. (39), where l_i denotes the angular momentum of the initial atomic state]. By contrast, transfer of high angular momenta and significant multipolar contributions [terms with $l,l' \sim 20-50$ in Eq. (39)] characterize the hard collision mechanism.

Figure 2 shows the SDCS calculated with different target potentials as a function of the energy (ϵ) of the ejected electrons. First we focus on the high-energy region of the emission spectra. Good agreement is found among the theoretical results based on different single-particle potentials for both Ne and Ar targets if $\epsilon \gtrsim 100-150$ eV. Details of the calculations show that the different potentials produce very similar continuum orbitals and the evaluated transition amplitudes deviate only at the lower momentum-transfer values due to

differences in binding energies and in the electronic structures. However, at high electron energies contributions with small momentum transfer are irrelevant in the integrated amplitudes [54]; consequently the SDCS shows no dependence on the binding energies and on the electronic structure. The fact that the form of the interaction between the electron and target plays a negligible role in the production of high-energy electrons verifies the picture that the process can be interpreted as a binary collision between the projectile and a free electron [1,55]. The target nucleus is only needed to localize the electron. Differences in the initial velocity distributions associated with the different target potentials are manifested in the double-differential electron ejection by changing the shape, and shifting the positions of the characteristic binary collision peak. However, they are washed out in the SDCS because of the integration over the ejection angle.

The situation is different at low electron energies. In low-energy ionization an essential part of the total energy transfer is associated with the binding energy. Therefore, the binding energy is considered as an essential scaling parameter for low-energy electron ejection [1]. In the present case the low-energy SDCS's show a strong dependence on the static potential applied in the calculation. However, this dependence cannot solely be attributed to the differences in the initial binding energies since the SDCS's for Ne are almost identical when evaluated with HFS and OPM potentials [Fig. 2(a)], although the eigenvalues of the $2p$ electrons differ by 20%. Moreover, for Ar the SDCS shows a similar structure (shoulder) around $\epsilon = 5-10$ eV, if HFS and LDA potentials are utilized and the SDCS's are almost identically obtained with the three potentials at the ionization threshold, while the corresponding $3p$ eigenvalues deviate from each other significantly (cf. Fig. 1).

Similar features can also be observed in SDCS's with different potentials in $B1$ calculations. This means that differences in some other characteristic parameters of the wave functions must also have strong effects on the calculated cross sections. These can be studied in more detail by multidifferential ejection patterns, as discussed below.

One can also study the role of the individual components of the static potential. Only small changes in the SDCS's are observed if one neglects the correlation part of the LDA potential. On the other hand, a strong, monotonic increase appears in the SDCS's with decreasing electron energies if the exchange part is also omitted. It is interesting to note that the shoulder observed in the SDCS for Ar with the LDA potential [Fig. 2(b)] disappears in this calculation, and can thus be attributed to LDA exchange.

Recommended experimental results [2] are also included in Fig. 2. The experiments are well represented by the calculations based on the OPM potential for both targets. The agreement obtained with the other potentials is less convincing. SDCS's obtained with the LDA potentials clearly overestimate the measurements for both Ne and Ar targets, thus emphasizing the importance of using a correct electronic exchange potential. The results obtained with the HFS potential show no systematic pattern, as has already been observed in the case of the TCS for net ionization [11].

Further information on the effects of the different single-particle potentials can be given by extending the studies to
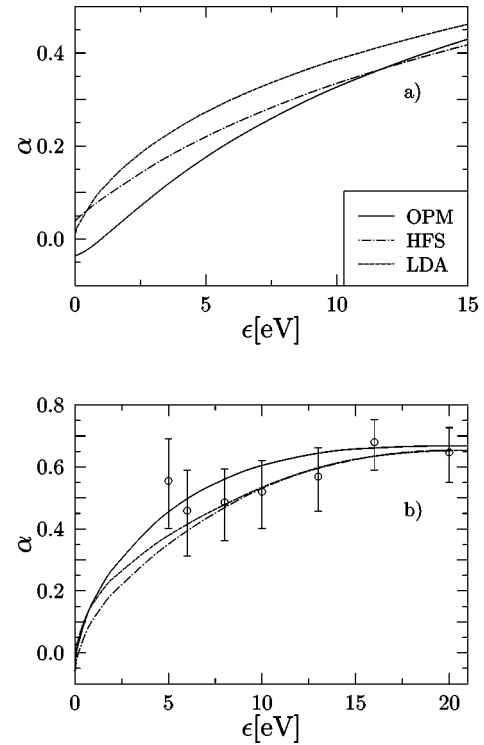

FIG. 3. Asymmetry parameter α as a function of electron energy for 300-keV H$^+$ impact on (a) Ne and (b) Ar. Lines: CDW-EIS calculation with different atomic potentials; ($\bigcirc$) experimental data estimated from Ref. [60].

the angular distribution of the electron emission. In the following we concentrate on low-energy electrons whose angular distribution is commonly characterized by anisotropy parameters [56,57]. As a further restriction, we investigate only the forward-backward asymmetry of the angular distribution described by the parameter

$$\alpha(\epsilon) = \frac{S(0) - S(\pi)}{S(0) + S(\pi)}, \qquad (47)$$

where $S(\theta)$ denotes the cross section at ejection angle θ and at fixed ϵ. In Fig. 3 we present results for α as a function of the electron energy. Independent of the single-particle potentials, the asymmetry increases with increasing electron energy. This is mainly due to the TCE's included in the CDW-EIS model, which have been discussed in detail elsewhere [1,58].

The asymmetry parameters presented in Fig. 3 are determined from the total electron yield. In these total α values the asymmetry character of a given orbital is emphasized or suppressed according to its relative contribution to the total yield. Our calculations show that the total asymmetries are mostly formed by the competition between the outer np_0 and np_1 orbitals. The individual orbitals reveal a different dependence on the different static potentials. For example, the asymmetries from the Ne($2p_1$) levels are less sensitive to the applied potentials than the ones from the $2p_0$ orbitals, and the situation is reversed for Ar($3p$) levels. This might explain why the results presented in Fig. 3 show no systematic behavior among the different potentials for the different targets. The differences among the alpha parameters associated
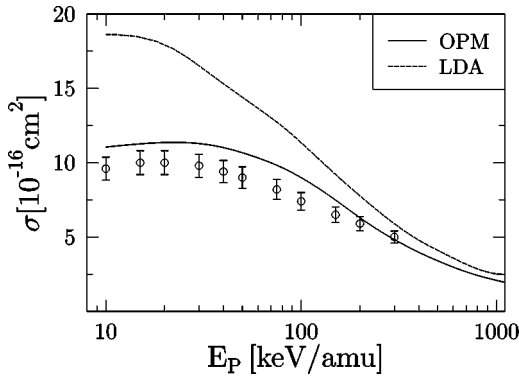
FIG. 4. Net electron-loss cross section as a function of impact energy for $He^{2+}+Ne$. Lines: BGM calculations with different atomic potentials; ($\bigcirc$) experimental data taken from Ref. [60].

FIG. 5. Weighted net electron loss as a function of the impact parameter for $He^{2+}+$ Ne at $E_P=10$ keV/amu. BGM calculations with different atomic potentials.

with the different potentials change with the strength of the projectile field or with the TCE's. For example, in a collision with a $Q_P=20$ projectile the asymmetry increases; however, no differences appear among results obtained with different potentials. In the present collision system a comparison of the results obtained from the $B1$ and the CDW-EIS calculations shows that the differences among the α values related to different potentials are two times larger in the case of the $B1$ approximation than the corresponding ones from the CDW-EIS theory. This means that the projectile and target fields are almost equally important for forming the asymmetry.

For Ar the experimental results, estimated from the measurement of Ref. [59], are included in Fig. 3(b). All three theoretical results are within the experimental error bars and more accurate measurements are required to clarify the situation.

B. Capture processes in $He^{2+}+Ne$ collisions

In this section we investigate the scattering system He^{2+} $+Ne$ by means of the BGM employing OPM and LDA atomic potentials. In addition, we have performed calculations with an OPM potential, in which the correlation contribution was turned off. As the results obtained with this exchange-only OPM are equal to the ones obtained with the OPM including the Colle-Salvetti correlation functional, we do not show them in the figures. The basis set used in the coupled-channel calculations includes the *KLM* shell eigenstates of the unperturbed Hamiltonian $\hat{h}_0$ [Eq. (32)] and BGM states $\{|\chi_s^\mu\rangle\}$ to the order $\mu=8$.

Figure 4 shows TCS's for net electron loss obtained with OPM and LDA potentials, respectively. Results obtained with the OPM potential are in good agreement with the experimental data in the whole energy range shown, whereas the LDA potential leads to considerably larger TCS's. Since the OPM potential provides a more accurate description of the unperturbed atomic system, we conclude that the net electron loss is mainly determined by the *static* (target) potential, i.e., the response part δv_{ee} of v_{ee} Eq. (5) is of minor importance, even at the smallest impact energy of 10 keV/amu.

At high energies, where net electron loss is dominated by ionization [60,61], the calculated TCS's reflect the binding
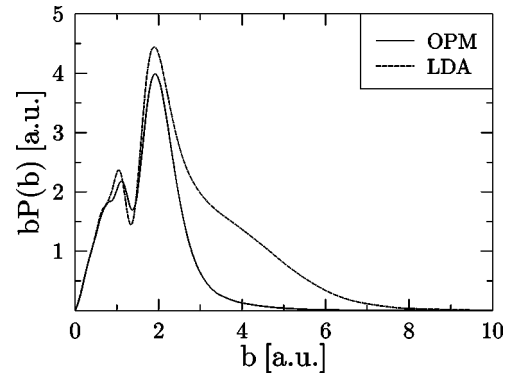
properties of the static potential used. As a consequence of the exact inclusion of the attractive exchange effects in the OPM potential, the electrons are bound more strongly than in the LDA potential, and thus the ionization yields are smaller.

At lower impact energies the situation is not that obvious, since electron capture, which is the dominant process, strongly depends on energy differences and on intermediate couplings between the initial target and the final projectile states. In order to analyze the different TCS obtained with OPM and LDA potentials at 10 keV/amu, we show the electron-loss probabilities weighted with the impact parameter b in Figs. 5 and 6. The net electron loss is very similar in both cases for small impact parameters, but for $b \gtrsim 3$ a.u. the LDA potential leads to substantial contributions to the TCS, whereas the net electron loss obtained from the OPM potential decreases very rapidly with increasing b. The individual loss probabilities from the different initial states (Fig. 6) show that this is due to the different behavior of the $2p$
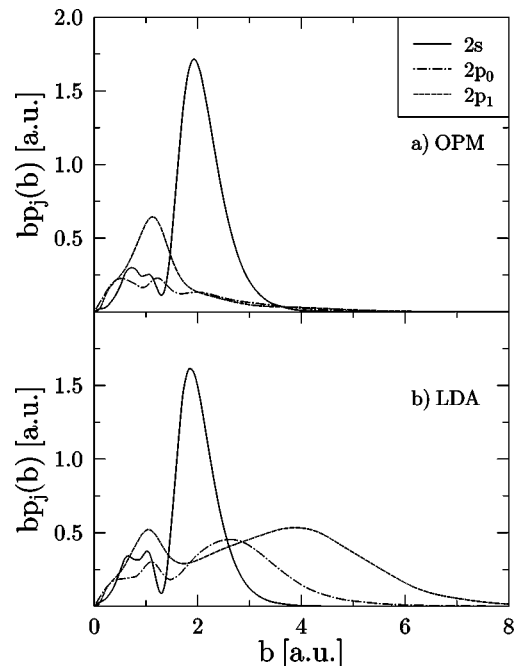

FIG. 6. Weighted single-electron-loss probabilities as functions of the impact parameter for $He^{2+}+Ne$ at $E_P=10$ keV/amu. BGM calculations with (a) OPM and (b) LDA potentials.
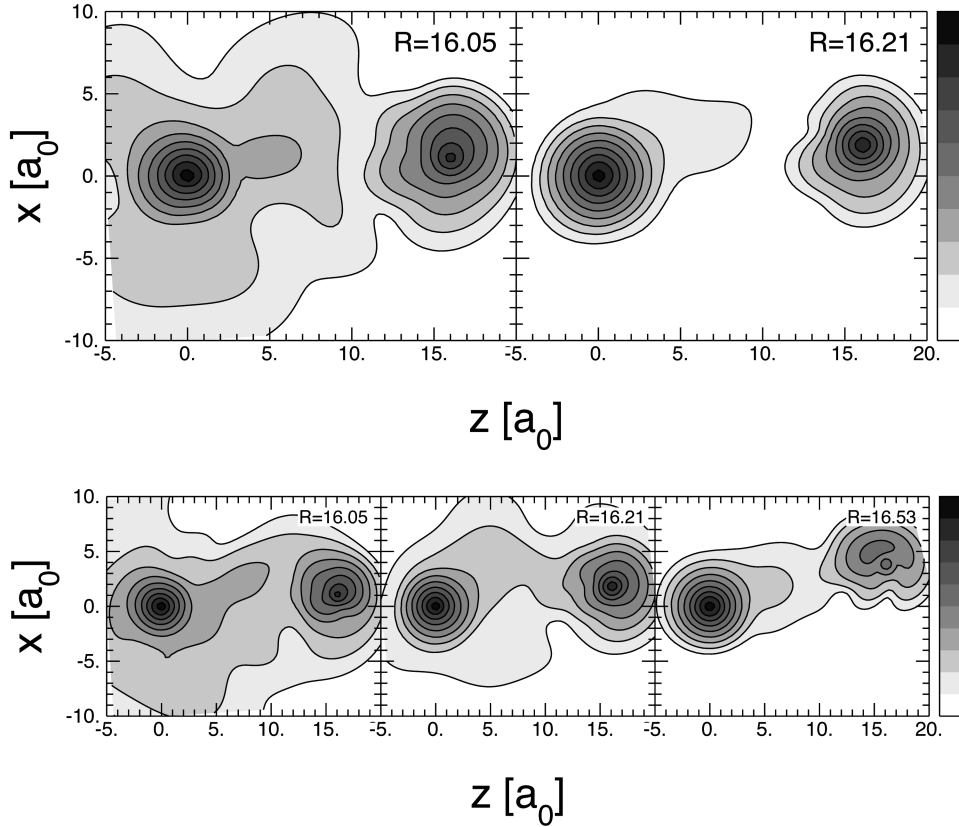
FIG. 7. Integrated one-particle density after the collision for $He^{2+} + Ne$ at $E_P = 10$ keV/amu. The target center is situated at the origin of the reference frame. The projectile center is situated at the coordinates $b,0,z=16$ a.u. The contours are scaled logarithmically. BGM calculations with (a) OPM potential at $b=1.1$ and 1.9 a.u., and (b) LDA potential at $b=1.05$, 1.85, and 4.0 a.u.

electrons. By contrast, the single-electron loss from the $2s$ level, which is responsible for the pronounced peak in the net electron-loss curve around $b=2$ a.u., shows the same pattern for both potentials.

Further insight into the different mechanisms is provided by consideration of the one-particle density after the collision process. Figure 7 displays densities that are integrated over the axis perpendicular to the scattering plane for some characteristic impact parameters. Around $b=1$ a.u., where all L-shell electrons contribute to net electron loss (cf. Fig. 6), the calculations with both LDA and OPM potentials show target ionization as well as capture. The spatial distribution of the continuum electrons is, however, somewhat different. Around $b=2$ a.u. ionization is less pronounced and almost completely suppressed in the case of the OPM potential. The main contribution to the net electron loss, which is due to the incoming $Ne(2s)$ electrons (cf. Fig. 6), can be interpreted as capture into the helium ground state. This conclusion is supported by the larger energy differences between the $Ne(2s)$ level and excited projectile states which indicates that corresponding transitions are not likely to occur.

At $b=4$ a.u. the electron loss obtained from the calculation with the LDA potential can be interpreted as capture into excited, nonspherical projectile states [Fig. 7(b)]. This process is caused by the small difference between the LDA energy of the neon $2p$ level ($\epsilon_{Ne(2p)}^{LDA} = -0.58$ a.u.) and the L-shell energy of He^+ ($\epsilon_{He^+(n=2)} = -0.5$ a.u.), and does not occur if the OPM potential is used ($\epsilon_{Ne(2p)}^{OPM} = -0.88$ a.u.). Since the TCS obtained with the OPM potential agrees rather well with experiment (cf. Fig. 4), it is evident that the

electron-loss process at large impact parameters predicted in LDA is an artifact caused by the deficiencies of the LDA potential.

Next, we consider q-fold electron-loss probabilities for the case of the OPM potential. Figure 8 shows results at 10 keV/amu obtained with both inclusive probability theory [Eq. (25)] and the binomial formulas (27) and (29). It can be seen that the details of the impact parameter dependence are lost step by step if first the Pauli principle is neglected [Eq. (27)], and then the shell structure is ignored [Eq. (29)]. In particular, at $b=1.9$ a.u., where the net electron loss has its maximum (cf. Fig. 5), the inclusive probability formalism shows that one- and three-electron loss is suppressed in favor of two-electron loss. If one combines this feature with the respective density plot [Fig. 7(a)], one can infer that capture of two electrons into the $He(1s^2)$ state is the process, which contributes almost exclusively at this impact parameter. This result is blurred by the simplifications used in Eqs. (27) and (29).

With increasing projectile velocity the sharp structures in the q fold electron-loss probabilities disappear, and the evaluation based on inclusive probability theory approaches the results obtained with the binomial formulas. This corresponds to the decreasing importance of capture processes. When electron loss is dominated by ionization, the Pauli exclusion principle does not influence the results because of the larger density of accessible continuum states.

Finally, we present ratios of double to single- and triple- to single-electron loss, R_2 and R_3, as functions of the impact energy in Fig. 9. Our results for R_2 agree well with the

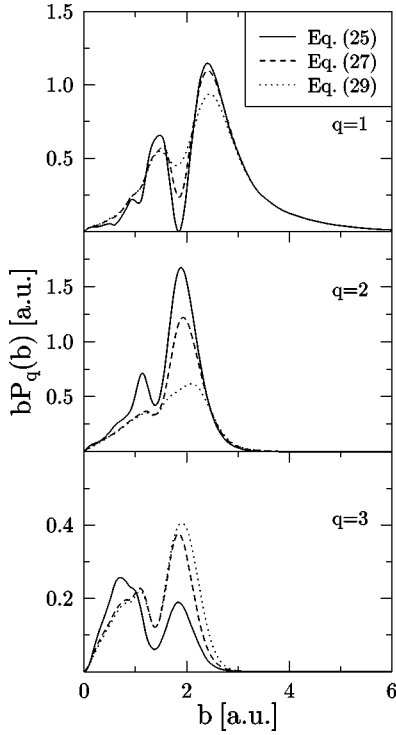FIG. 8. Weighted q-electron-loss probabilities (evaluated according to the cited equations) as functions of the impact parameter for $He^{2+}+Ne$ at $E_P = 10$ keV/amu. BGM calculations with OPM potential.

FIG. 9. Cross-section ratios $R_2 = \sigma_2/\sigma_1$, $R_3 = \sigma_3/\sigma_1$ as functions of impact energy for $He^{2+}+Ne$. Lines: BGM calculations with the OPM potential; experimental data: (○) taken from Ref. [61]; (●) taken from Ref. [62].

experimental data over the whole energy range shown, whereas the calculated R_3's are too large except at the highest impact energies. A reduction of these ratios may be expected in particular at lower energies if the response part δv_{ee} of v_{ee} [Eq. (5)] would be taken into account in the dynamical calculations. The change of the electronic density will both screen the projectile and unscreen the target nucleus, so that *multiple* electron loss will be lowered. This would also lead to slightly smaller net electron-loss cross sections, which could then be in even closer agreement with the experimental data than the results shown in Fig. 4.

At high energies, K-shell ionization with subsequent Auger processes may contribute to the multiple-ionization TCS. Following Ref. [62] we assume that the electronic relaxation subsequent to K-shell vacancy production is independent of the actual scattering process. With this assumption we can estimate these contributions to the twofold and threefold electron-loss probabilities via

$$P_q = P_0^K P_q^L + \alpha_1 P_1^K P_{q-2}^L + \alpha_2 P_1^K P_{q-3}^L, \quad q=2,3, \quad (48)$$

where the q-fold loss probabilities from the K and L shell P_q^K and P_q^L are computed according to Eq. (27), and $\alpha_1 = 0.74$ and $\alpha_2 = 0.22$ are the branching ratios for KLL and $KLLL$ Auger decay as given in Ref. [63]. The ratios R_2 and R_3 plotted in Fig. 9 show that Auger processes contribute only very little to two-electron loss, but there is an indication that they determine the three-electron-loss TCS at impact energies greater than 1 MeV/amu more strongly.

C. Ionization of neon by antiprotons

In this section we investigate the ionization of neon by antiprotons with the static OPM potential, and compare the
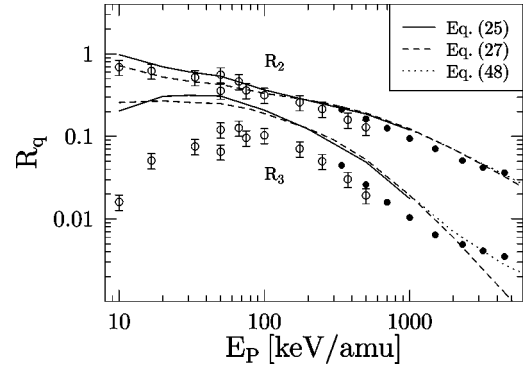
theoretical results with new experimental data in the energy range 30–1000 keV [54]. For the BGM calculations we utilize the same basis set as described in Sec. III B. Since capture processes do not occur in this collision system, electron-loss TCS's obtained with the BGM can directly be compared with the corresponding CDW-EIS results for ionization.

In Fig. 10(a), we compare our results for net ionization with experimental values, which have been obtained from the published one-, two-, and three-electron ionization TCS's [53] according to

$$\sigma_{net} \approx \sigma_1 + 2\sigma_2 + 3\sigma_3. \quad (49)$$

At energies larger than 300 keV both CDW-EIS and BGM results are in good agreement with the experimental data, although they deviate slightly from each other and seem to merge only for $E_P > 1$ MeV. At lower energies, they show quite different patterns. While the TCS's obtained with the BGM continually increase with decreasing impact velocity, the CDW-EIS calculations result in a maximum around 100 keV, which appears to be too large compared with experiment. However, it is difficult to establish the general behavior of the experimental cross sections at the lower energies.

Furthermore, we have calculated q-fold ionization according to Eq. (27) with single-particle probabilities obtained from both methods. For BGM solutions, we have checked that inclusive probability theory [Eq. (25)] leads to the same results, as expected from the arguments given in Sec. III B. Figures 10(b)–10(d) display one-, two-, and three-electron-ionization TCS's. For the one-electron ionization the overall agreement between experiment and both theories is good. Both calculations do not show a double-peak structure between 200 and 300 keV for which the experimental results give some indication. Again, as already seen in the net ionization, the maximum of the CDW-EIS cross sections around 130 keV seems to be too large. The BGM leads to a smaller peak, slightly shifted to lower energies. Both curves cross around 50 keV, the CDW-EIS cross sections falling off more steeply toward low energies.

For two- and three-electron ionization we obtain comparable results with both methods at impact energies $E_P \gtrsim 100$ keV. At the highest energies, where multiple ionization is commonly explained by interference effects between various amplitudes of the Born perturbation series [7,53,62], the ex-
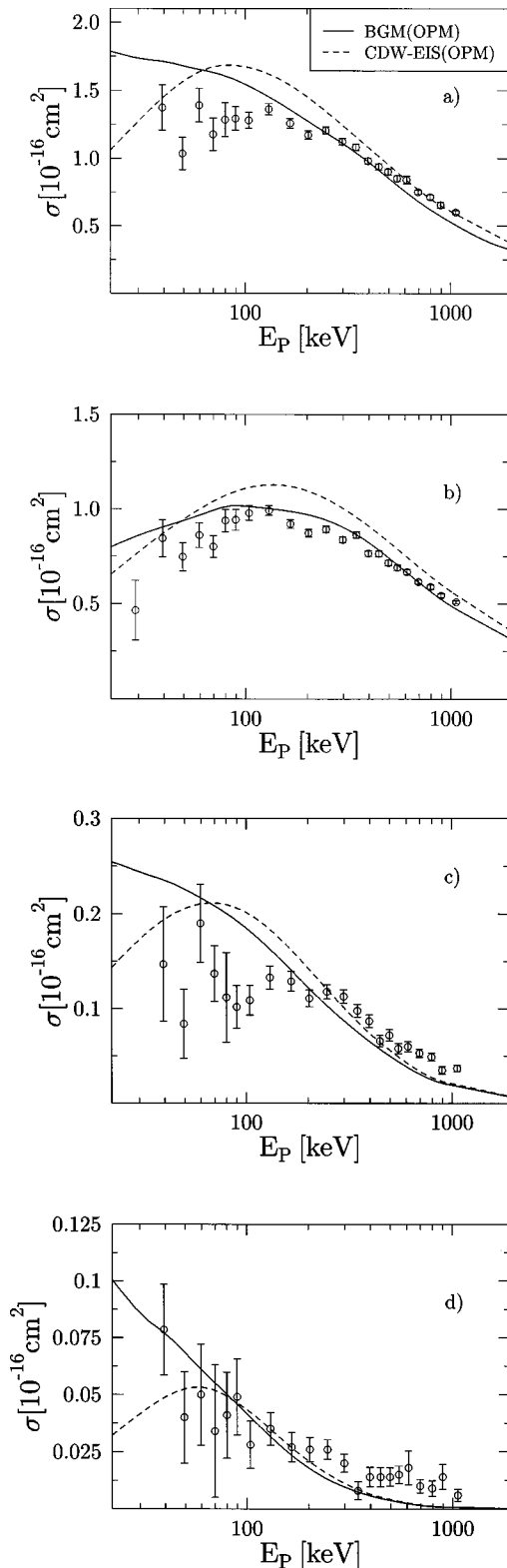
FIG. 10. Net and q-electron ionization cross sections as functions of impact energy for $\bar{p}$ + Ne for (a) net ionization, (b) $q=1$, (c) $q=2$, and (d) $q=3$. Lines: calculations with the OPM potential; ($\bigcirc$) experimental data taken from Ref. [53].

perimental TCS's are larger than our theoretical results. Further analysis of our model is required for an understanding of these deviations.

A striking feature of our two- and three-electron ioniza-

tion results is the different low-energy behavior obtained with the two methods. Whereas the CDW-EIS curves show a maximum around 50–70 keV, similar to the case of one-electron ionization, the BGM results exhibit no peak structure and continually increase toward low energies. Unfortunately, no ultimate conclusions can be drawn from the low-energy behavior of the experimental TCS's due to their large statistical errors.

At even smaller impact energies one can understand the collision dynamics by means of the correlation diagram of the corresponding quasimolecule. In order to elucidate the properties of our model in more detail, we calculated single-particle energies of the two-center Hamiltonian (31) as functions of the internuclear distance R. The important result of this analysis is, that the $\sigma(\mathrm{Ne}(2p_0))$ and $\pi(\mathrm{Ne}(2p_1))$ energy levels become positive for internuclear distances $R \lesssim 1.2$ a.u. Thus the $\mathrm{Ne}(2p)$ electrons are unbound in very slow close collisions if the dynamics is described by the Hamiltonian (31), in which the electronic density is not adiabatically relaxed in the combined field of target and projectile nuclei because of the neglect of δv_{ee} in v_{ee} [Eq. (5)]. Nevertheless, the CDW-EIS ionization TCS's fall off at low projectile energies, and therefore indicate the decreasing reliability of the method for slow collisions. By contrast, the increasing multiple-ionization TCS's obtained with the BGM correctly reflect the properties of the single-particle Hamiltonian used. Obviously, these properties are physically not correct in the present example, since the united-atom limit $(R\rightarrow 0)$ corresponds to the formation of an F^- ion which is stable. It is thus necessary to take the response part δv_{ee} of v_{ee} [Eq. (5)] into account in order to describe slow collisions for which the correlation diagram becomes meaningful.

IV. CONCLUDING REMARKS

In this work we have investigated collisions between bare ions and the rare-gas atoms neon and argon on the basis of an effective single-particle picture, employing local potentials which account for static exchange-correlation effects on different levels of approximation. The OPM approach yields the best local representation of the exchange potential, in contrast to HFS and LDA approaches which rely on different versions of the density dependence of the homogeneous electron gas. The response of the effective electron-electron interaction in the presence of the projectile has been neglected. We have applied two methods, CDW-EIS and BGM, for the solution of the ensuing set of single-particle equations in order to analyze the role of static potential effects from different points of view.

Both methods lead to the general conclusion that electron loss and ionization can be properly described if the OPM potential is used. Total cross sections for net electron loss are fully determined by the static potential for a wide range of impact energies, whereas response effects are not important even for rather slow collisions for which the velocity of the projectile is smaller than typical orbital velocities of the active electrons. Moreover, the OPM potential also permits one to calculate differential ionization cross sections which are in fair agreement with experimental data, as has been shown by means of CDW-EIS calculations.

By contrast, HFS and LDA potentials yield less reliable

results for these scattering processes, and give rise to artificial structures. For $p+Ar$ collisions the CDW-EIS results obtained with HFS and LDA potentials exhibit shoulders in the SDCS's which can be traced back to the inadequate description of exchange effects. Furthermore, a detailed analysis by means of the BGM has shown that the LDA potential leads to an unphysical capture contribution in $He^{2+}+Ne$ collisions at large impact parameters. These results confirm our previous conclusion that it is important to account accurately for static exchange if one aims at a quantitative understanding of inelastic scattering processes.

Moreover, we have shown in the present work that multiple-electron-loss probabilities reflect the Pauli exclusion principle if capture processes contribute. In these cases the widely used binomial and multinomial formulas are not sufficient and have to be replaced by the corresponding results based on the inclusive probability formalism. At intermediate and high impact energies we obtain good agreement with experimental data for q-fold electron loss and ionization of Ne by antiprotons and He^{2+} ions. An extension of the present investigation to the study of collisions between *highly* charged ions and atoms will be published elsewhere.

The limitations of our basic assumption—the neglect of the response part of the effective electron-electron potential—may become apparent in the q-fold electron-loss cross sections at small impact energies. For the scattering of antiprotons from neon atoms this is evident for nearly adiabatic situations since the stability of the $(\bar{p},Ne)$ compound in the united-atom limit cannot be represented with a frozen atomic target potential.

Inclusion of such effects in terms of an approximate time-dependent optimized potential seems feasible. The BGM permits the calculation of the one-particle density at any given intermediate time step for which the OPM integral equation has to be solved. Given the results of the present work, this combination of the BGM with the time-dependent OPM seems to provide a promising framework for the more detailed study of correlated time-dependent many-electron dynamics.

[1] N. Stolterfoht, R. D. DuBois, and R. D. Rivarola, *Electron Emission in Heavy Ion-Atom Collisions*, Springer Series on Atoms and Plasmas Vol. 20 (Springer, Berlin, 1997).

[2] M. E. Rudd, Y.-K. Kim, D. H. Madison, and T. J. Gay, Rev. Mod. Phys. **64**, 441 (1992).

[3] M. E. Rudd, Y.-K. Kim, D. H. Madison, and J. W. Gallagher, Rev. Mod. Phys. **57**, 965 (1985).

[4] C. L. Cocke and R. E. Olson, Phys. Rep. **205**, 153 (1991).

[5] J. Ullrich, R. Moshammer, R. Dörner, O. Jagutzki, V. Mergel, H. Schymidt-Böcking, and L. Spielberger, J. Phys. B **30**, 2917 (1997).

[6] J. H. McGuire, N. Berrah, R. J. Bartlett, J. A. R. Samson, J. A. Tanis, C. L. Cocke, and A. S. Schlachter, J. Phys. B **28**, 913 (1995).

[7] H. Knudsen and J. F. Reading, Phys. Rep. **212**, 107 (1992).

[8] M. Horbatsch, J. Phys. B **25**, 3797 (1992); R. E. Olson, J. Ullrich, and H. Schmidt-Böcking, *ibid.* **20**, L809 (1987); R. E. Olson, in *Electronic and Atomic Collisions*, edited by H. B. Gilbody, W. R. Newell, F. H. Read, and A. C. H. Smith (Elsevier, Amsterdam, 1988), pp. 271–285.

[9] N. M. Kabachnik, V. N. Kondratyev, Z. Roller-Lutz, and H. O. Lutz, Phys. Rev. A **56**, 2848 (1997).

[10] M. Horbatsch, Phys. Rev. A **49**, 4556 (1994).

[11] T. Kirchner, L. Gulyás, H. J. Lüdde, A. Henne, E. Engel, and R. M. Dreizler, Phys. Rev. Lett. **79**, 1658 (1997).

[12] P. D. Fainstein, V. H. Ponce, and R. D. Rivarola, J. Phys. B **22**, 1207 (1989).

[13] M. McCartney and D. S. F. Crothers, J. Phys. B **26**, 4561 (1993).

[14] L. Gulyás, P. D. Fainstein, and A. Salin, J. Phys. B **28**, 245 (1995).

[15] H. J. Lüdde, M. Horbatsch, A. Henne, and R. M. Dreizler, Phys. Lett. A **145**, 173 (1990).

[16] E. Runge and E. K. U. Gross, Phys. Rev. Lett. **52**, 997 (1984).

[17] E. K. U. Gross, J. F. Dobson, and M. Petersilka, in *Topics in Current Chemistry*, edited by R. F. Nalewajski (Springer, Heidelberg, 1996), Vol. 181, p. 81; C. A. Ullrich and E. K. U. Gross, Comments At. Mol. Phys. **33**, 211 (1997).

[18] D. S. F. Crothers and J. F. McCann, J. Phys. B **16**, 3229 (1983).

[19] P. D. Fainstein, V. H. Ponce, and R. D. Rivarola, J. Phys. B **24**, 3091 (1991).

[20] H. J. Lüdde, A. Henne, T. Kirchner, and R. M. Dreizler, J. Phys. B **29**, 4423 (1996).

[21] O. J. Kroneisen, H. J. Lüdde, T. Kirchner, and R. M. Dreizler, J. Phys. A (to be published).

[22] A. Henne, H. J. Lüdde, and R. M. Dreizler, J. Phys. B **30**, L565 (1997).

[23] A. Görling, Phys. Rev. A **55**, 2630 (1997).

[24] J. F. Dobson, M. J. Bünner, and E. K. U. Gross, Phys. Rev. Lett. **79**, 1905 (1997).

[25] W. Kohn and L. J. Sham, Phys. Rev. **140**, A1133 (1965).

[26] J. C. Slater, Phys. Rev. **81**, 385 (1951).

[27] S. H. Vosko, L. Wilk, and M. Nusair, Can. J. Phys. **58**, 1200 (1980).

[28] B. Y. Tong and L. J. Sham, Phys. Rev. **144**, 1 (1966); R. D. Cowan, A. C. Larson, D. Liberman, J. B. Mann, and J. Waber, *ibid.* **144**, 5 (1966).

[29] E. Engel, J. A. Chevary, L. D. Macdonald, and S. H. Vosko, Z. Phys. D **23**, 7 (1992).

[30] A. D. Becke, Phys. Rev. A **38**, 3098 (1988); C. Lee, W. Yang, and R. G. Parr, Phys. Rev. B **37**, 785 (1988); J. P. Perdew, in

Electronic Structure of Solids 1991, edited by P. Ziesche and H. Eschrig (Akademie Verlag, Berlin, 1991), p. 11.

[31] A. D. Becke, J. Chem. Phys. **96**, 2155 (1992).

[32] R. M. Dreizler and E. K. U. Gross, *Density Functional Theory* (Springer, Berlin, 1990).

[33] A. Görling and M. Levy, Phys. Rev. A **50**, 196 (1994); E. Engel, A. Facco Bonetti, S. Keller, I. Andrejkovics, and R. M. Dreizler, *ibid.* **58**, 964 (1998).

[34] R. Colle and O. Salvetti, Theor. Chim. Acta **37**, 329 (1975).

[35] J. D. Talman and W. F. Shadwick, Phys. Rev. A **14**, 36 (1976).

[36] J. B. Krieger, Y. Li, and G. J. Iafrate, Phys. Rev. A **45**, 101 (1992); E. Engel and S. H. Vosko, *ibid.* **47**, 2800 (1993).

[37] T. Kotani, Phys. Rev. Lett. **74**, 2989 (1995); D. M. Bylander and L. Kleinman, *ibid.* **74**, 3660 (1995); Phys. Rev. B **55**, 9432 (1997); M. Städe, J. A. Majewski, P. Vogl, and A. Görling, Phys. Rev. Lett. **79**, 2089 (1997).

[38] T. Grabo and E. K. U. Gross, Chem. Phys. Lett. **240**, 141 (1995).

[39] J. Chen and M. J. Stott, Phys. Lett. A **176**, 101 (1993).

[40] H. J. Lüdde and R. M. Dreizler, J. Phys. B **18**, 107 (1985).

[41] P. Kürpick, H. J. Lüdde, W. D. Sepp, and B. Fricke, Z. Phys. D **25**, 17 (1992).

[42] H. J. Lüdde, A. Macías, F. Martín, A. Ríera, and J. L. Sanz, J. Phys. B **28**, 4101 (1995).

[43] M. Horbatsch, Z. Phys. D Suppl. **21**, 63 (1991).

[44] R. D. DuBois and S. T. Manson, Phys. Rev. A **36**, 2585 (1987).

[45] I. Ben-Itzhak, T. J. Gray, J. C. Legg, and J. H. McGuire, Phys. Rev. A **37**, 3685 (1988).

[46] Dž Belkić, J. Phys. B **11**, 3529 (1978).

[47] N. Stolterfoht *et al.*, Europhys. Lett. **4**, 899 (1987).

[48] P. D. Fainstein, V. H. Ponce, and R. D. Rivarola, J. Phys. B **21**, 287 (1988).

[49] E. Clementi and C. Roetti, At. Data Nucl. Data Tables **14**, 177 (1974).

[50] S. T. Manson, L. H. Toburen, and N. Stolterfoht, Phys. Rev. A **12**, 60 (1975).

[51] P. D. Fainstein, L. Gulyás, and A. Salin, J. Phys. B **29**, 1225 (1996).

[52] R. M. Dreizler, l. F. Errea, A. Henne, H. J. Lüdde, A. Ríera, and P. Sánchez, Phys. Rev. A **47**, 3852 (1993).

[53] K. Paludan, H. Bluhme, H. Knudsen, U. Mikkelsen, S. P. Møllet, E. Uggerhøj, and E. Morenzoni, J. Phys. B **30**, 3951 (1997).

[54] M. Inokuti, Rev. Mod. Phys. **43**, 297 (1971).

[55] T. F. M. Bonsen and L. Vriens, Physica (Amsterdam) **47**, 307 (1970).

[56] W. Meckbach, I. B. Nemirowsky, and C. Garibotti, Phys. Rev. A **24**, 1793 (1981).

[57] J. Burgdörfer, Phys. Rev. A **33**, 1578 (1986).

[58] P. D. Fainstein, L. Gulyás, F. Martín, and A. Salin, Phys. Rev. A **53**, 3243 (1996).

[59] M. E. Rudd, L. H. Toburen, and N. Stolterfoht, At. Data Nucl. Data Tables **23**, 405 (1979).

[60] M. E. Rudd, T. V. Goffe, and A. Itoh, Phys. Rev. A **32**, 2128 (1985).

[61] R. D. DuBois, Phys. Rev. A **36**, 2585 (1987).

[62] L. H. Andersen, P. Hvelplund, H. Knudsen, S. P. Møller, A. H. Sørensen, K. Elsener, K.-G. Rensfelt, and E. Uggerhøj, Phys. Rev. A **36**, 3612 (1987).

[63] T. A. Carlson, W. E. Hunt, and M. O. Krause, Phys. Rev. **151**, 41 (1966).